



# Modulating the active sites of nickel phosphorous by pulse-reverse electrodeposition for improving electrochemical water splitting

Byung Keun Kim<sup>a</sup>, Myung Jun Kim<sup>b,\*</sup>, Jae Jeong Kim<sup>a,\*</sup>

<sup>a</sup> School of Chemical and Biological Engineering, Institute of Chemical Processes, Seoul National University, Gwanak 1, Gwanak-ro, Gwanak-gu, Seoul 08826, Republic of Korea

<sup>b</sup> Department of Applied Chemistry, Kyung Hee University, Yongin-si, Gyeonggi-do 17104, Republic of Korea

## ARTICLE INFO

### Keywords:

Nickel phosphorus  
Pulse-reverse electrodeposition  
Hydrogen evolution reaction (HER)  
Oxygen evolution reaction (OER)  
Mott-Schottky plot

## ABSTRACT

This study introduces how pulse-reverse electrodeposition (PRED) affects the properties of nickel phosphorus (NiP) films and improves the performance of hydrogen evolution reaction (HER) and oxygen evolution reaction (OER). The impact of electrochemical parameters in PRED on HER and OER activities is explored, indicating that changes in two activities of PRED dissolution step are opposite. An increase in dissolution amount during PRED enhances OER while decreasing HER activity. The Mott-Schottky analysis reveals that improvement in HER by adopting PRED is due to an increase in the reactivity of active sites. On the contrary, OER is enhanced due to the number of active sites on the surface of NiP films increased by the excess dissolution during PRED. Surface analyses suggest that the opposite response of HER and OER is caused by different factors; uniform formation of NiP governs HER activity while removability of phosphate determines the exposure of OER-active Ni oxide phases.

## 1. Introduction

Environmental problems such as global warming have been pushing the development of clean and eco-friendly energy sources [1,2]. Electrochemical water splitting, one of the promising technologies to produce renewable energy sources, has been spotlighted which enables efficient production of hydrogen (H<sub>2</sub>). The electrochemical water splitting consists of two half-reactions; hydrogen evolution reaction (HER) and oxygen evolution reaction (OER). Although electrochemical water splitting is pollution-free and convenient, scaling up the electrochemical H<sub>2</sub> production system has been impeded due to the high maintenance cost. Noble metal electrocatalysts such as Pt, Ru, and Ir, which are recognized as the state-of-art HER and OER electrocatalysts [3], dramatically increase the H<sub>2</sub> production cost, dropping the economic efficiency of electrochemical water splitting. Therefore, many studies have been carried out to discover efficient water splitting electrocatalysts composed of non-precious transition metals such as Ni [4–7], Fe [8,9], and Co [10,11]. To overcome the intrinsically poor performance of non-noble metal electrocatalysts (vs. noble metals), alloying of aforementioned metals with other metals [12–15] or non-metal elements such as phosphorus [10,16], chalcogenides [17,18], and carbides [19] attracted great attention to enhanced electrocatalytic activity and

durability.

Nickel phosphorus (NiP) has been widely acknowledged as an outstanding water splitting electrocatalyst because of its excellent electrocatalytic activity and cost-effectiveness [20–22]. It was also reported that controlling the P content is the most critical to HER and OER activities of NiP. Relatively metal-rich NiP exhibits superior activity toward OER, while relatively high P content enhances HER activity [23, 24]. Tuning the electronic state of Ni by P doping drops free energy of water dissociation ( $\Delta G_{H_2O}$ ) and hydrogen adsorption free energy ( $\Delta G_{H^+}$ ) [25]. As a result, the energy barrier for HER is diminished, facilitating H<sub>2</sub> formation and eventually promoting overall HER performance [26, 27]. On the other hand, phosphorus in NiP acts as a good supporting layer beneath the surface Ni oxide or oxyhydroxide during the OER, while P on the outermost surface needs to be removed [28,29]. In addition, various synthetic methods were developed to maximize the HER and OER activities of NiP electrocatalysts by manipulating the characteristic of the active sites. Various NiP shapes including nanoparticles [30], nanosheets [31], and more complicated urchin-like structures [32] have been reported in previous studies.

Electrodeposition, one of the NiP synthetic methods, has been widely adopted since this method is inexpensive and easy to form film-type electrocatalysts over a wide area with good adhesion [33,34].

\* Corresponding authors.

E-mail addresses: [myungjun.kim@khu.ac.kr](mailto:myungjun.kim@khu.ac.kr) (M.J. Kim), [jjkimm@snu.ac.kr](mailto:jjkimm@snu.ac.kr) (J.J. Kim).

<https://doi.org/10.1016/j.apcatb.2022.121226>

Received 17 November 2021; Received in revised form 20 January 2022; Accepted 15 February 2022

Available online 18 February 2022

0926-3373/© 2022 Elsevier B.V. All rights reserved.

Furthermore, the surface morphology, P content, crystallinity, and amount of deposit can be simply changed by the applied potentials, the concentrations of Ni precursor, and complexing agents. The previous studies intensively researched the effect of electrodeposition parameters on the NiP properties and HER/OER activities, the overall performance of NiP for HER and OER is still limited compared to other electrocatalysts such as Pt and Ru [2,35]. Therefore, more studies to further improve the activities of NiP for HER and OER are required. Pulse-reverse electrodeposition (PRED), one of the electrodeposition methods, alternatively applies cathodic and anodic potentials to repeat deposition and dissolution of electrodeposits. This electrodeposition method is more powerful to control the properties of electrodeposits compared to constant potential deposition (CPD) or constant current deposition. For Cu electrodeposition, the surface roughness and grain size of Cu films were easily controlled by modulating the anodic steps in PRED [36,37]. In addition, the surface adsorption of chemicals can be controlled by anodic steps, eventually changing the film properties and morphology of Cu deposits [37,38]. In a similar way, the introduction of PRED for NiP formation can provide more room to modify the properties of NiP by adjusting additional parameters in PRED such as reverse potential and time.

This study shows the effects of the electrochemical parameters in PRED on the properties of the NiP films and the HER and OER activities. The parameters of the PRED were first optimized based on the HER/OER activities, showing that the introduction of PRED to NiP formation could carry the catalytic properties of NiP films to the activities of the state-of-art electrocatalysts. It was also observed that the changing tendency of HER and OER activities according to the dissolution step in the PRED was found to be the opposite. Increasing the dissolution amount during the PRED enhanced the OER activity of NiP films while reducing the HER activity. The Mott-Schottky analyses and X-ray photoelectron spectroscopy (XPS) revealed that the opposite response of the HER and OER activities was related to the characteristics and the number of active sites on the NiP films. The PRED modulated the chemical states of P in the NiP films, determining the HER/OER activities.

## 2. Experimental methods

### 2.1. Electrodeposition of NiP films

A three-electrode standard electrochemical cell was used to perform the NiP electrodeposition. A Cu rotating disk electrode (RDE) or Cu foil pasted on the RDE was used as a substrate for NiP electrodeposition. A geometric area of the RDE and foil was  $0.1257 \text{ cm}^2$ . A Pt wire and a saturated calomel electrode (SCE, KCl saturated) were selected as counter and reference electrodes, respectively. The electrochemical measurements and electrodeposition processes were carried out with a potentiostat (PATSTAT<sup>TM</sup> MC, Princeton Applied Research).

Before the electrodeposition, the surface native oxide of Cu was removed by cyclic voltammetry in an aqueous solution with 0.1 M citric acid. Oxide removal was performed by cycling the potential from 0.00 V (vs. OCP) to  $-1.50 \text{ V}$  (vs. SCE) at a scan rate of  $50 \text{ mV/s}$  for five times. The aqueous electrolyte for NiP electrodeposition consisted of 50 mM nickel sulfate ( $\text{NiSO}_4 \cdot 6\text{H}_2\text{O}$ ), 150 mM sodium hypophosphite ( $\text{NaH}_2\text{PO}_2$ ), and 150 mM ethylenediamine. In a constant potential deposition (CPD) process, the constant potential of  $-0.90 \text{ V}$  (vs. RHE) was applied, and the deposition amount was fixed to  $20 \text{ C/cm}^2$ . PRED consisted of on and reverse periods. The cathodic deposition potential ( $E_{\text{on}}$ ) during on time was fixed at  $-0.90 \text{ V}$  (vs. RHE). The lengths of on time ( $t_{\text{on}}$ ) and reverse time ( $t_{\text{rev}}$ ), and the reverse potential ( $E_{\text{rev}}$ ) were varied, and their detailed conditions were presented in each figure. The  $t_{\text{on}}$ ,  $t_{\text{rev}}$ , and  $E_{\text{rev}}$  were changed from 1 s to 7 s, from 0.5 s to 9 s, and from  $-0.30 \text{ V}$  to  $0.30 \text{ V}$  (vs. RHE). Note that the  $E_{\text{rev}}$  examined in this study induced the anodic current during the PRED. The total deposition amount was controlled by the total charges including both on and reverse steps ( $20 \text{ C/cm}^2$ , identical to the condition for CPD).

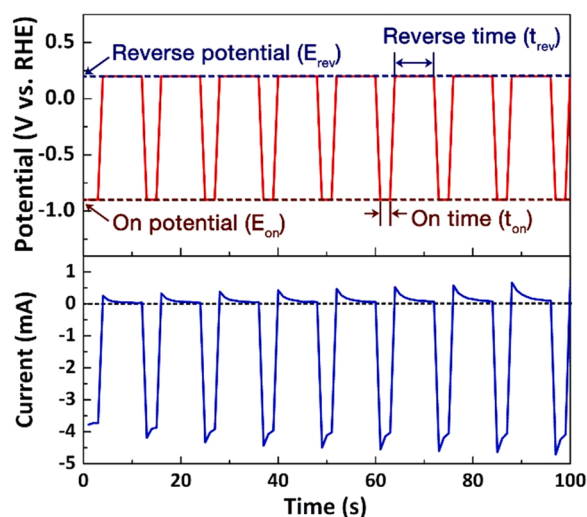


Fig. 1. A waveform of potential and the corresponding current response for PRED with the definitions of reverse potential ( $E_{\text{rev}}$ ), reverse time ( $t_{\text{rev}}$ ), on potential ( $E_{\text{on}}$ ), and on time ( $t_{\text{on}}$ ).

### 2.2. Characterization of NiP films

Field emission scanning electron microscopy (FE-SEM, Merlin Compact, ZEISS) and energy-dispersive X-ray spectroscopy (EDS, Merlin Compact, ZEISS) were utilized to investigate surface morphologies and element distributions, respectively. X-ray photoelectron spectroscopy (XPS, Sigma Probe, VG Scientific) was used for comparing the electronic structures of NiP films. The XPS spectra were calibrated with the location of C 1s peak (binding energy:  $284.8 \text{ eV}$ ). The crystal structure of the NiP films was investigated by X-ray Diffraction (XRD, D8-Advance, Bruker). For electrochemical surface area (ECSA) measurement, cyclic voltammetry was carried out in the potential range from  $-0.05 \text{ V}$  to  $0.05 \text{ V}$  (vs. OCP) with varying the scan rates from  $10 \text{ mV/s}$  to  $50 \text{ mV/s}$ .

### 2.3. Electrochemical measurements for hydrogen and oxygen evolution on NiP films

A three-electrode system for the electrochemical measurement consisted of the NiP films as a working electrode, a Pt wire as a counter electrode, and an SCE as a reference electrode. Note that we confirmed that the experiment with a graphite anode was identical to that with a Pt counter electrode, indicating the electrocatalytic performance of NiP films was not critically affected by Pt dissolution/redeposition for the conditions examined in this study. Furthermore, it was confirmed the stability of the SCE in  $1.0 \text{ M KOH}$  solution was enough for our experiments. The potential difference for the SCE during the experiment was confirmed as smaller than  $10 \text{ mV}$ . The electrolyte for the HER and OER was  $1.0 \text{ M KOH}$  ( $\text{pH} = 13.88$ ). The electrode potentials were converted to present the values with respect to a reversible hydrogen electrode (RHE) ( $E_{\text{RHE}} = E_{\text{SCE}} + 0.242 + 0.05916 \times \text{pH}$ ). The validity of  $0.242 \text{ V}$  for our SCE was checked by cyclic voltammetry with SCE as a working electrode and a Pt wire as a counter electrode in  $\text{H}_2$ -saturated  $0.5 \text{ M H}_2\text{SO}_4$  ( $25^\circ\text{C}$ ), indicating that the potential value for the SCE was between  $0.234$  and  $0.239 \text{ V}$  (i.e.,  $3\text{--}8 \text{ mV}$  difference vs.  $0.242 \text{ V}$ ). Since such a small difference was not critical in our experiments, the value of  $0.242 \text{ V}$  was used in our study. Linear sweep voltammetry was performed by sweeping the electrode potential from  $0.2 \text{ V}$  to  $-0.4 \text{ V}$  (vs. RHE) for HER and from  $1.2 \text{ V}$  to  $1.7 \text{ V}$  (vs. RHE) for OER. The scan rate for both measurements was  $2 \text{ mV/s}$ . Electrochemical impedance spectroscopy (EIS) was performed to obtain the charge transfer resistance ( $R_{\text{CT}}$ ) for HER and OER. The frequency varied from  $100 \text{ kHz}$  to  $0.1 \text{ Hz}$  with an amplitude of  $10 \text{ mV}$ , superimposed to the overpotential of  $-205$

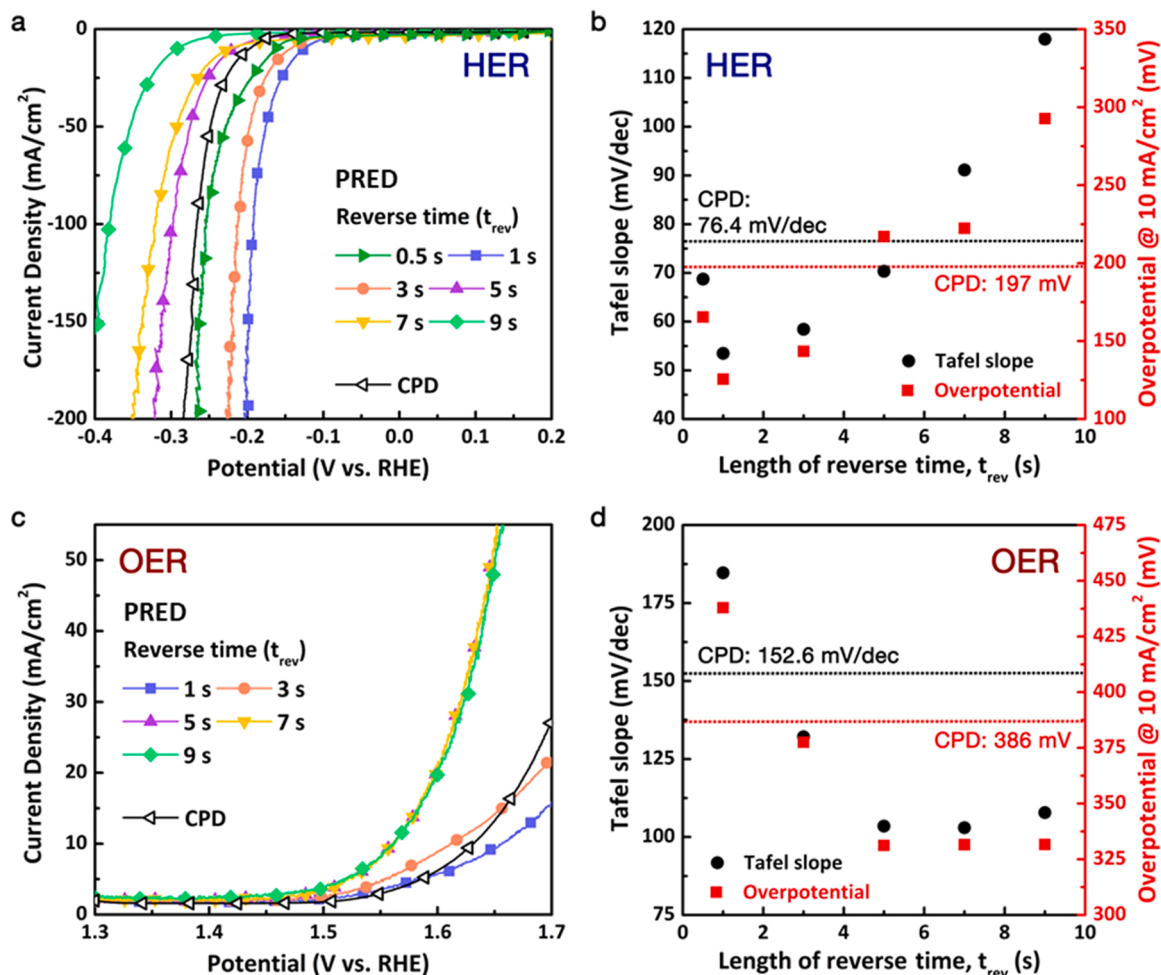


**Fig. 2.** (a) Polarization curves and (b) the overpotential at  $-10 \text{ mA/cm}^2$  and Tafel slope for HER on the NiP films deposited by PRED with varying the  $t_{rev}$ . (c) Polarization curves and (d) the overpotential at  $10 \text{ mA/cm}^2$  and Tafel slope for OER on the NiP films deposited by PRED with varying the  $t_{rev}$ . The length of  $t_{on}$  and applied  $E_{rev}$  were 3 s and 0.0 V, respectively.

mV for HER and 340 mV for OER, respectively. A full-cell test was performed for 24 hrs with a two-electrode system consisting of two NiP films to compare the performance of the NiP films prepared by CPD and the optimum PRED and also check the stability of NiP films. The current density and electrolyte for the long-term test were  $20 \text{ mA/cm}^2$  and 1.0 M KOH, respectively. Mott-Schottky plot was obtained at the frequency of 1000 Hz with the potential range from 0.47 V to  $-0.13 \text{ V}$  (vs. RHE) for HER, and from 1.07 V to 1.67 V (vs. RHE) for OER. The interval between each point was set as 25 mV. The relative slopes used in the figures were calculated as the slope for the NiP films from the PRED divided by the slope for the NiP film from the CPD.

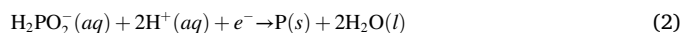
### 3. Results and discussion

#### 3.1. Water splitting performance of NiP films deposited by pulse-reverse electrodeposition

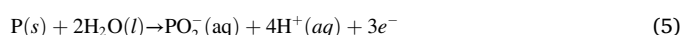
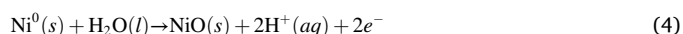
A representative potential waveform of PRED is presented in Fig. 1. The PRED consisted of two steps: on and reverse steps. The NiP was deposited in the on period, and its dissolution took place in the reverse period. This study examined the effects of the length of on time ( $t_{on}$ ), reverse time ( $t_{rev}$ ), and the reverse potential ( $E_{rev}$ ) on the HER and OER activities of NiP films. The current response during PRED shown at the bottom of Fig. 1 indicates the cathodic and anodic currents passed during each step, and the anodic charge in the reverse step was significantly smaller than that for the on step. The main purpose of the reverse

step was to change the chemical states of P after depositing a large amount of NiP in the on period. Therefore, a large change in the surface roughness was intentionally prevented by applying a relatively small dissolution step. Since a large amount of anodic charge can also dramatically increase the surface roughness of electrodeposits [36,37], the HER and OER performance can be affected by the change in the surface roughness (i.e., electrochemically active surface area). The reduction and oxidation reactions during the PRED are listed below: [39–41].

Reduction reactions during  $t_{on}$ :



Oxidation reactions during  $t_{rev}$ :



The formation of P could be changed by both reduction and oxidation parameters in the PRED directly via reactions in Eqs. (2) and (5), and the redox reactions for Ni (Eqs. (1), (3), and (4)) simultaneously happening could also affect the incorporation of P into the Ni matrix. Therefore, this study explored the effects of PRED parameters on the

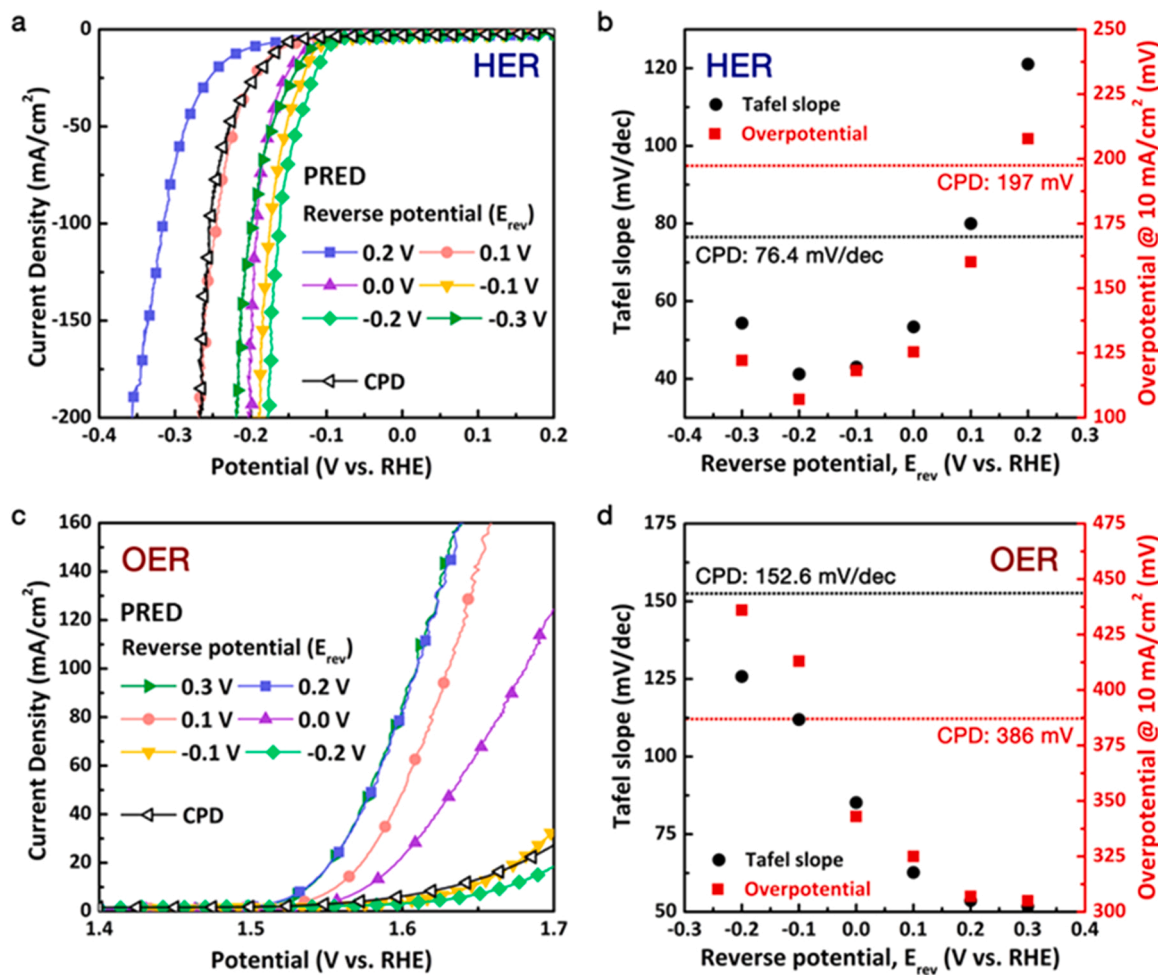


**Fig. 3.** (a) Polarization curves and (b) the overpotential at  $-10 \text{ mA/cm}^2$  and Tafel slope for HER on the NiP films deposited by PRED with varying the  $E_{rev}$  at the  $t_{on}$  of 3 s and  $t_{rev}$  of 1 s. (c) Polarization curves and (d) the overpotential at  $10 \text{ mA/cm}^2$  and Tafel slope for OER on the NiP films deposited by PRED with varying the  $E_{rev}$  at the  $t_{on}$  of 3 s and  $t_{rev}$  of 9 s.

chemical states of P and the corresponding electrocatalytic activities of NiP films for water splitting.

Figs. S1, 2, and 3 show the changes in the HER and OER activities of NiP films according to the  $t_{on}$ ,  $t_{rev}$ , and  $E_{rev}$  of PRED, respectively. Fig. 2a and b indicate enhanced activities of the NiP films prepared with the  $t_{rev}$  shorter than 3 s, compared to CPD. The most active NiP film was obtained at the  $t_{rev}$  of 1 s, and the Tafel slope and the overpotential at  $-10 \text{ mA/cm}^2$  were decreased by 22.9 mV/dec and 71.3 mV compared to the case of CPD, respectively. On the contrary, the HER activity was increased when the length of the  $t_{on}$  increases (Fig. S1a and b). Both HER activity improvement with the decrease in  $t_{rev}$  (Fig. 2a and b) and the increase in the  $t_{on}$  (Fig. S1a and b) suggest that minimal dissolution during PRED was beneficial for HER. Note that the HER activity at  $t_{rev} = 0.5$  was worse than that at  $t_{rev} = 1.0$  s. It was most likely due to that the dissolution amount at  $t_{rev} = 0.5$  was too small to obtain the advantage of PRED.

On the contrary, the change in the OER performance with  $t_{rev}$  and  $t_{on}$  was opposite to the results for HER. Fig. 2c and d show that an increase in the  $t_{rev}$  improves the OER activity of the NiP films. When the  $t_{rev}$  exceeded 3 s, the OER activity was higher than that from CPD, and the performance was saturated at the  $t_{rev}$  longer than 5 s. In the optimum range of  $t_{rev} > 5$  s, the Tafel slope and the overpotential at  $10 \text{ mA/cm}^2$  were 49.4 mV/dec and 55.1 mV (on average) lower than the results of CPD, respectively. On the contrary, the OER performances as a function of the  $t_{on}$  showed volcanic behavior (Fig. S1d). At the  $t_{on}$  of 3 s, the best OER performance was observed, and as the  $t_{on}$  exceeded the optimum

$t_{on}$ , the OER performance deteriorated. Two results indicate that more dissolution (shorter  $t_{on}$  or longer  $t_{rev}$ ) during PRED was advantageous to improve the OER performance, which was an opposite behavior observed in the HER.

The results observed in Figs. S1 and 2 suggest that the dissolution amount was critical for the HER and OER activities of NiP films. The  $E_{rev}$  was the other parameter that determined the dissolution amount in the reverse period. More positive  $E_{rev}$  increased the dissolution amount during PRED. Therefore, the HER and OER activities were investigated with varying the  $E_{rev}$  to verify the trends observed in the results discussed above. Note that the experiments for  $E_{rev}$  were performed at different  $t_{rev}$ , 1 s for HER and 9 s for OER since the trend of optimum  $t_{rev}$  was opposite for HER and OER (Fig. 2). Fig. 3a and b show the HER performance of NiP films as the  $E_{rev}$  changed from  $-0.3 \text{ V}$  to  $0.2 \text{ V}$ . Except for the case of  $-0.3 \text{ V}$ , the changes in  $E_{rev}$  to the negative values (less dissolution during the reverse period) increased the HER activity of NiP films. The exception at  $-0.3 \text{ V}$  was similar to the result at  $t_{rev} = 0.5$  observed in Fig. 2b. Since the insufficient dissolution at relatively negative  $E_{rev}$  (Fig. 3b) or short  $t_{rev}$  (Fig. 2b) limited the benefit of PRED, the HER performance of NiP films at these conditions was between those from the optimum PRED and CPD. On the contrary, the opposite trend was observed with the OER. More positive  $E_{rev}$  (more dissolution during the reverse period) was found to improve the OER activity of NiP films. These trends were in good agreement with the results for varying  $t_{on}$  and  $t_{rev}$  shown in Figs. S1 and 2. The Nyquist plots and the charge transfer resistance ( $R_{CT}$ ) are presented in Fig. S2 (HER) and S3 (OER), also



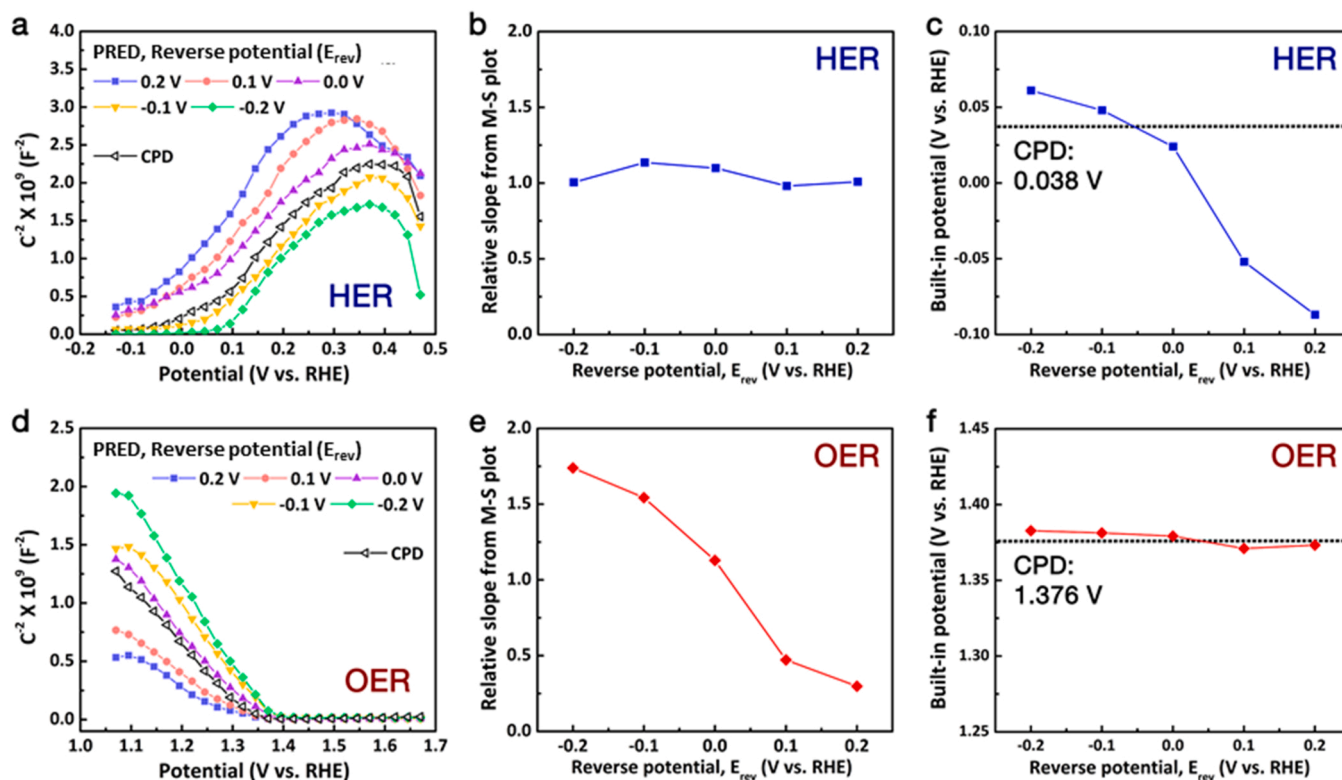


Fig. 4. (a) Mott-Schottky plot, (b) relative slope, and (c) built-in potential for HER on NiP films deposited with varying the  $E_{rev}$ . The  $t_{rev}$ ,  $E_{on}$ , and  $t_{on}$  were 1 s,  $-0.9 \text{ V}$ , and 3 s, respectively. (d) Mott-Schottky plot, (e) relative slope, and (f) built-in potential for OER on NiP films deposited with varying the  $E_{rev}$ . The  $t_{rev}$ ,  $E_{on}$ , and  $t_{on}$  were 9 s,  $-0.9 \text{ V}$ , and 3 s, respectively.

showing the same trends observed in Fig. 3.

The reverse steps in PRED were found to be effective to modulate the properties of NiP films and improve the HER and OER activities of NiP films; however, the reverse step has opposite effects on the HER and OER performance. The maximum improvement in HER activity was achieved at the minimal dissolution (shorter  $t_{rev}$ , longer  $t_{on}$ , and more negative  $E_{rev}$ ) in the reverse step while the OER was promoted when dissolution amount was increased (longer  $t_{rev}$ , shorter  $t_{on}$ , and more positive  $E_{rev}$ ). Through three sets of experiments, the optimum conditions,  $t_{on} / t_{rev} / E_{rev}$ , were found to be 3 s / 1 s /  $-0.2 \text{ V}$  for HER and 3 s / 9 s /  $0.2 \text{ V}$  for OER. At the optimum conditions, the Tafel slope and the overpotential at  $-10 \text{ mA/cm}^2$  were 41.2 mV/dec and 107 mV for HER (CPD: 76.4 mV/dec, 197 mV) and 51.7 mV/dec and 305 mV for OER (CPD: 152.4 mV/dec, 386 mV). The full-cell test was further performed to observe the advantage of NiP films prepared by PRED and to check the stability of the NiP films (Fig. S4). The results indicate that the cell potential (at  $20 \text{ mA/cm}^2$ ) from the two NiP films prepared at each optimum condition of PRED for HER and OER was decreased by 0.13 V compared to two NiP films prepared by the CPD. For both cases, the potential increase for 24 hrs was only 11 mV, implying the strong stability of the NiP films deposited by the electrodeposition method. The performances of NiP films were compared to the state-of-art film type electrocatalysts. Note that only film-type electrocatalysts were chosen for the comparison to exclude the effects of surface morphology and microscopic surface area on the electrocatalytic activities. As summarized in Table S2, the HER activity of the NiP film from PRED ranked high, compared to the state-of-art electrocatalysts. Although the OER performance was not in the top ranks, the PRED NiP film was comparable with various alloyed electrocatalysts (Table S3). Such an improvement in HER and OER performance of NiP films without adding other components in the NiP matrix demonstrated the advantages of PRED.

### 3.2. Characterization and Mott-Schottky analysis of NiP films correlated with water splitting performance

The investigation on film properties was further conducted to reveal how PRED improved the NiP activities to the HER and OER. The electrochemically active surface area (ECSA), the film composition, Ni and P distributions, the surface density of active sites, and the electronic/chemical state of P in NiP films can potentially be affected by the parameters in the PRED. Also, these properties can change the electrocatalytic activities of NiP films. Our characterization results revealed (please see below) that except for the number of active sites and the chemical state of P, other properties were not significantly changed by PRED for the conditions examined in this study.

The distributions of Ni and P in NiP films prepared by CPD and PRED are presented in Fig. S5a. The SEM images show that the surface morphology of NiP films from two deposition methods was comparable, and the mapping results indicate that both Ni and P were uniformly distributed for two cases. Furthermore, as displayed in Fig. S5b, the P contents in the NiP films from CPD and PRED were in a small range of 14.5 and 16.2 at%. Moreover, the ECSA of six different films from CPD and PRED, estimated from the non-Faradaic currents (Fig. S6a), shows only a 4.1% difference (Fig. S6b). Furthermore, the AFM analyses revealed that the root-mean-square surface roughness for NiP films prepared by CPD and PRED ( $t_{on} = 3.0 \text{ s}$ ,  $E_{rev} = 0.0 \text{ V}$ ,  $t_{rev} = 7.0 \text{ s}$ ) were 23 and 29 nm. Since the original surface roughness of Cu foil was 16 nm, the surface area change due to the PRED was not critical in our study. The crystal structures of the NiP films were further investigated by XRD (Fig. S7). The XRD patterns indicate that the NiP films prepared by both CPD and PRED were amorphous. These results indicate that the P contents and surface morphology were not critically changed by introducing PRED, and these factors did not critically determine the HER and OER activities of NiP films.

The characteristics of active sites for HER and OER were investigated

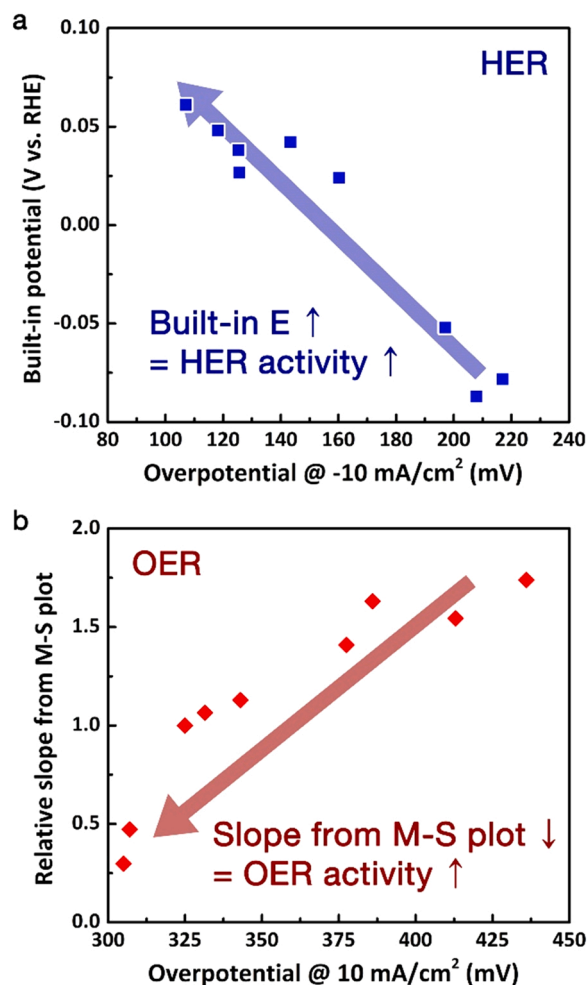


Fig. 5. Correlation of (a) built-in potential and overpotential at -10 mA/cm<sup>2</sup> for HER and (b) the relative slope and overpotential at 10 mA/cm<sup>2</sup> for OER.

by the Mott-Schottky analysis [42–44]. The Mott-Schottky (M-S) plot is a plot of the reciprocal of the square of capacitance ( $1/C^2$ ) vs. potential bias (V) [45]. The Mott-Schottky equation is given as follow (Eq. (6)),

$$\frac{1}{C^2} = \frac{2}{qA^2\epsilon N_D} (V + V_{bi}) \quad (6)$$

where  $C$  is capacitance,  $q$  is the elementary charge,  $A$  is surface area,  $\epsilon$  is permittivity,  $N_D$  is doping density,  $V$  is electrode potential, and  $V_{bi}$  is built-in potential. This plot has been widely used for semiconductor electrochemistry to investigate the energy diagram at the semiconductor/electrolyte junction [45–47]. The slope of the M-S plot gives the doping density of the semiconductor interface, while the x-intercept provides the built-in potential, (or the flat-band potential) [46,47]. Furthermore, this method can be used for characterizing the surface states of electrocatalysts [48–51]. Considering the NiP film/electrolyte interphase, the slope from the M-S plot can be used for characterizing the active sites for HER and OER. Since the reciprocal of the slope is related to the doping concentration for the semiconductor, it is strongly related to the number of vacancy sites for electrocatalysts, which can act as the active sites for HER and OER [47]. On the other hand, the built-in potential (x-intercept of the M-S plot represents) describes the energy barrier for the electrochemical reaction. Therefore, the built-in potential corresponds to how much the active sites on NiP films are favorable for the reactions [46,47].

As shown in Fig. 3, the HER and OER activities of NiP films were unidirectionally changed with  $E_{rev}$  of PRED, i.e., more negative  $E_{rev}$

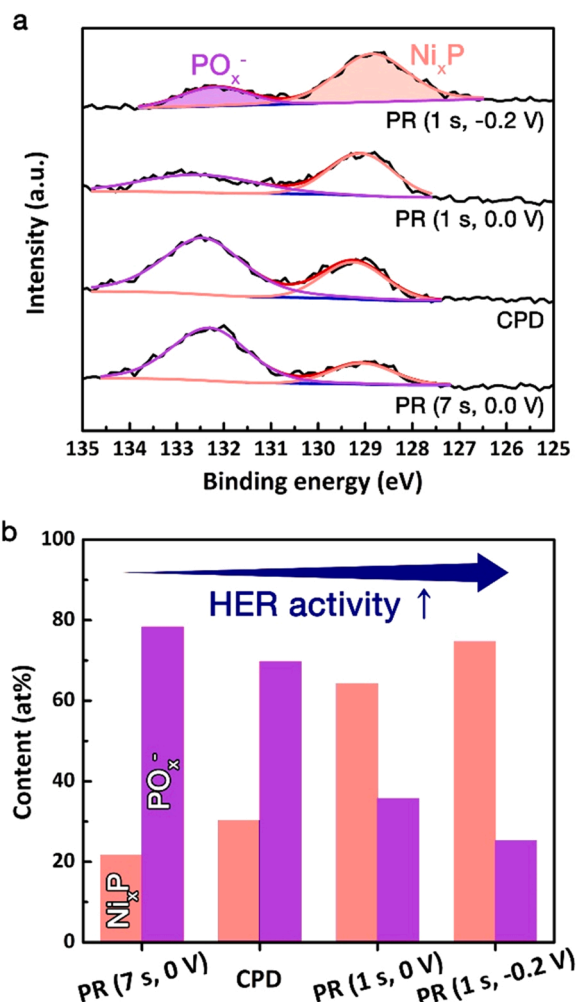


Fig. 6. (a) P 2p spectra of as-deposited NiP films, and (b) a change in the composition of P states upon PRED conditions. The numbers in parenthesis for PR correspond to the length of  $t_{rev}$  and applied  $E_{rev}$ . The  $E_{on}$  and  $t_{on}$  were -0.90 V and 1 s, respectively.

increased HER activities while decreasing OER performance. Therefore, the M-S analyses were performed with this set of PRED to estimate the changes in the active sites of NiP films [48,50]. Fig. S8 describes the procedure to obtain the slope and built-in potential from the M-S plots for HER and OER. Note that the slopes from the NiP films prepared by PRED were normalized by the slope from the CPD, called relative slope in this study. Fig. 4a shows the M-S plot for HER, indicating a clear positive shift of the M-S plot with more negative  $E_{rev}$ . The positive slope of the M-S plot implies that the NiP films behaved like an n-type semiconductor for HER. As shown in the M-S plot, the slopes were not changed with the  $E_{rev}$  (Fig. 4b) while the built-in potential was changed to the positive values with more negative  $E_{rev}$  (Fig. 4c). On the contrary, the M-S plots for OER with a negative slope indicate that the NiP films acted as a p-type semiconductor (Fig. 4d). Opposite to the results for HER, the slope of the M-S plot decreased with more positive  $E_{rev}$  (Fig. 4e) while the built-in potentials were unchanged (Fig. 4f).

The opposite behavior observed in the M-S plots implied that the factors determining the electrocatalytic activities were different for HER and OER. The changes in the built-in potential were most likely to be relevant to the HER activity of NiP films while the slopes from the M-S plots might be related to the OER activity. To verify this hypothesis, more M-S analyses were performed at the different conditions of PRED (Fig. S9), and the correlations of the built-in potential vs. HER activity and the slope from the M-S plots vs. OER activity were created by

combining all data. Fig. 5a clearly indicates that the overpotential required for  $-10 \text{ mA/cm}^2$  current density decreased with more positive built-in potential, meaning higher HER activity. Plotting the Tafel slope instead of the overpotential (Fig. S10a) also showed an increase in the HER activity when the built-in potential was shifted to the positive values. In the case of OER, a decrease in the slope from the M-S plots was connected to the improvement in the OER activity, i.e., lower overpotentials at  $10 \text{ mA/cm}^2$  (Fig. 5b) and a smaller Tafel slope (Fig. S10b).

The correlation of the electrocatalytic activities and the results of the M-S analyses suggests that the HER activity was determined by the characteristics of the active sites on the NiP films. Since the built-in potential was related to the reactivity of the active sites, the improvement in the HER activity (Fig. 5a) was due to the fact that the PRED with minimal dissolution (at shorter  $t_{\text{rev}}$  or more negative  $E_{\text{rev}}$ , see Figs. 2a, b, 3a and b) increased the reactivity of the active sites. Since the slope was not changed with  $E_{\text{rev}}$  (Fig. 4b), the number of active sites for HER was not significantly changed by the PRED. On the contrary, the OER activity was determined by the number of active sites because the lower values for the reciprocal of the M-S plot slope correlated to the higher OER activity. This relationship implies that the PRED with more dissolution (at longer  $t_{\text{rev}}$  or more positive  $E_{\text{rev}}$ , see Figs. 2c, d, 3c and d) increased the number of the active sites on the NiP films, leading to the increase in the OER activity of the NiP films.

### 3.3. Modulation of the chemical states of P with pulse-reverse electrodeposition improving water splitting performance of NiP films

From the correlation of the M-S analyses and electrocatalytic activities, it was found that the PRED at less dissolution increases the reactivity of active sites for HER while more dissolution increases the number of active sites for OER. Since the analytical results discussed above could not answer which surface chemistry is responsible for the activity change, intensive surface analyses were performed by XPS. It was observed that the chemical states of Ni (Fig. S11) and P (Fig. 6) were significantly changed by the PRED. When minimal dissolution occurred during the PRED (the top of Fig. 6a), the formation of  $\text{Ni}_3\text{P}$  was enhanced compared to the result of CPD. Since the resistance of  $\text{Ni}_3\text{P}$  to the dissolution was higher than the pure Ni [52,53], the dissolution steps in the PRED can selectively remove the pure Ni phase, leading to an increase in the portion of  $\text{Ni}_3\text{P}$ . However, at longer  $t_{\text{rev}}$  and more positive  $E_{\text{rev}}$  (Fig. 6a), more phosphate form (marked as  $\text{PO}_x^-$ ) was detected. This result indicates that the dissolution step in the PRED promoted the oxidation of P in the  $\text{Ni}_3\text{P}$  phase to form  $\text{PO}_x^-$  when excessive anodic charges were passed.

The contents of  $\text{Ni}_3\text{P}$  and  $\text{PO}_x^-$  estimated from Fig. 6a are summarized in Fig. 6b. It was observed that the HER activity increased as the fraction of  $\text{Ni}_3\text{P}$  increased while that of  $\text{PO}_x^-$  decreased. Fig. S11b also indicated that the HER activity increased with the portion of  $\text{Ni}_3\text{P}$  over pure Ni. The same amount of P was incorporated into these NiP films (Fig. S4b); therefore, the NiP films with more  $\text{PO}_x^-$  should contain more pure Ni phase (or  $\text{Ni}_3\text{P}$  phase with less P), matched to the results in Fig. S11b. Since the  $\text{Ni}_3\text{P}$  was found to be more active than pure Ni [25,53], enhanced uniformity of  $\text{Ni}_3\text{P}$  (with less  $\text{PO}_x^-$ ) deposited by the PRED led to a higher HER activity. Therefore, the positive shift of the built-in potential (an increase in the reactivity of active sites) at more negative  $E_{\text{rev}}$  (Fig. 4c) can be explained by the increase in the portion of  $\text{Ni}_3\text{P}$  (vs. pure Ni). However, since both pure Ni and  $\text{Ni}_3\text{P}$  act as active sites for HER and the total number of active sites is the sum of pure Ni and  $\text{Ni}_3\text{P}$  sites, the slope from the M-S plot (Fig. 4b) was not changed due to the similar active surface area with Ni and  $\text{Ni}_3\text{P}$  in total.

The OER case was more complicated since the oxidative conditions during the OER changed the surface state. It was found that all kinds of Ni on the surface turned to  $\text{Ni}(\text{OH})_2$ ,  $\text{NiO}$ , and  $\text{NiOOH}$  after OER (Figs. S12a and b). In the case of P, as shown in Fig. S13a, more dissolution during PRED (at more positive  $E_{\text{rev}}$ ) increased the formation of  $\text{PO}_x^-$  compared to  $\text{Ni}_3\text{P}$ , which was the same behavior observed in

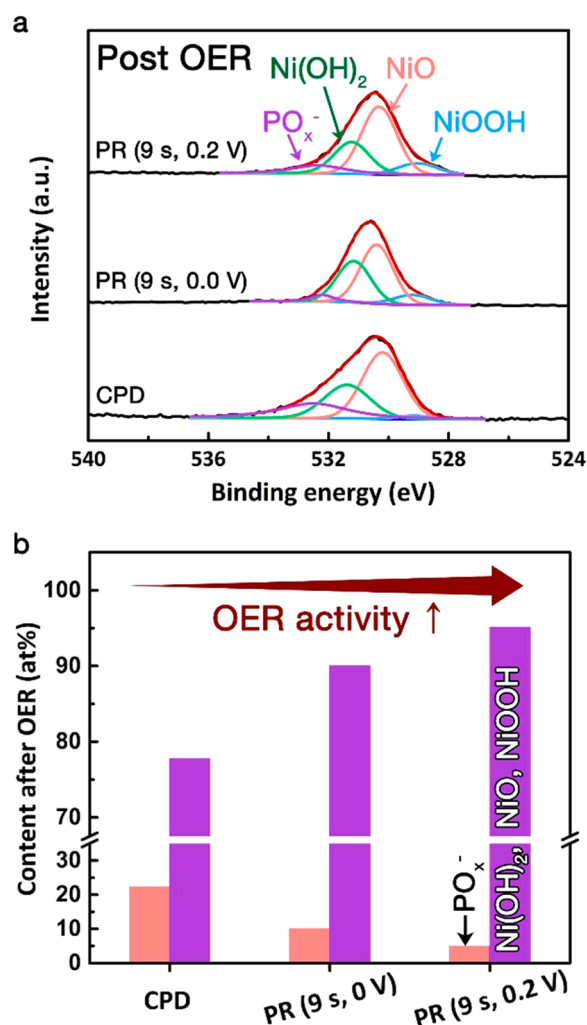


Fig. 7. (a) O 1s spectra of NiP films after OER, and (b) a change in the composition of O states upon PRED conditions. The numbers in parenthesis for PR correspond to length of  $t_{\text{rev}}$  and applied  $E_{\text{rev}}$ . The  $E_{\text{on}}$  and  $t_{\text{on}}$  were  $-0.9 \text{ V}$  and  $3 \text{ s}$ , respectively.

Fig. 6a. After the OER, it was found that the  $\text{Ni}_3\text{P}$  phase disappeared and only trace amount of  $\text{PO}_x^-$  phase remained (Fig. S13b). Interestingly, more  $\text{PO}_x^-$  survived when the as-deposited NiP film contained more  $\text{Ni}_3\text{P}$  and less  $\text{PO}_x^-$  (Fig. S13b). This behavior was supported by the spectra for O 1s shown in Fig. 7. It was observed that more  $\text{Ni}(\text{OH})_2$ ,  $\text{NiO}$ , and  $\text{NiOOH}$  formed over  $\text{PO}_x^-$  although less  $\text{Ni}_3\text{P}$  was initially exposed to the surface. Although the exact mechanism of this phenomenon was not clear, this behavior might be related to the peroxidation step of the NiP during the OER. As shown in Fig. S14, the voltammogram of NiP film deposited by CPD showed the first oxidation peak at  $0.34 \text{ V}$  (vs. RHE), which was related to the oxidation of  $\text{Ni}^0$  to  $\text{Ni}^{2+}$  (i.e.,  $\text{NiO}$ ) [54]. On the contrary, the NiP films from the PRED were first oxidized at  $0.92\text{--}0.93 \text{ V}$  (vs. RHE), which corresponds to the phosphorus oxidation to phosphate ( $\text{PO}_x^-$ ) [55]. Since XPS spectra in Fig. S13b showed that the NiP films from the PRED after OER contained less  $\text{PO}_x^-$ , the  $\text{PO}_x^-$  formed at  $0.92\text{--}0.93 \text{ V}$  might be easily detached from the surface, resulting in the exposure of more Ni on the film surface. This hypothesis was supported by that the oxidation peak at  $1.40 \text{ V}$  (vs. RHE) corresponding to the oxidation of  $\text{NiO}$  to  $\text{NiOOH}$  was enlarged in the cases of the NiP films from the PRED. In summary, the PRED with sufficient dissolution steps (longer  $t_{\text{rev}}$  or more positive  $E_{\text{rev}}$ ) changed the dissolution behavior of surface phosphorus, consequently forming more  $\text{Ni}(\text{OH})_2$ ,  $\text{NiO}$ , and  $\text{NiOOH}$  on the surface. This behavior was matched to the results from



the M-S analysis (Fig. 4e), which showed an increase in the number of active sites for OER from the change in the built-in potential.

#### 4. Conclusions

This study showed that the dissolution step in pulse-reverse electrodeposition can modulate the chemical states of P in the NiP films. It was found that enhancing the formation of  $\text{Ni}_x\text{P}$  with preventing the oxidation of P to  $\text{PO}_x^-$  was the effective way to maximizing the electrocatalytic activity of NiP films for hydrogen evolution reaction. Therefore, the dissolution step should be as little as possible to remove pure Ni, leading to a corresponding increase in the formation of a more active  $\text{Ni}_x\text{P}$  phase. On the contrary, the enhancement of the activity of NiP films for oxygen evolution reaction was achieved by changing the properties of  $\text{PO}_x^-$  to be easily removed before oxygen evolution. This phenomenon increased the number of active sites ( $\text{Ni}(\text{OH})_2$ , NiO, and  $\text{NiOOH}$ ) for oxygen evolution. Although the exact mechanism was not clarified, longer or stronger dissolution during pulse-reverse electrodeposition promoted the formation of removable  $\text{PO}_x^-$ , leading to the improvement in the overall oxygen evolution reaction properties. These results suggest that modulating the chemical states of P is one of the most critical factors determining the activities of HER/OER electrocatalysts. Therefore, the pulse-reverse electrodeposition methods would be advantageous to improve the electrocatalytic activities of other metal (or alloy) phosphorous. If the morphology of the P-modulated metal phosphorus is further modified to have a more active surface area, the product electrocatalysts will show competitive electrocatalytic activity for water splitting.

#### CRediT authorship contribution statement

**Byung Keun Kim:** Conceptualization, Conducting experiment, Data curation, Writing – original draft. **Myung Jun Kim:** Conceptualization, Supervision, Data curation, Writing – review & editing, Funding acquisition. **Jae Jeong Kim:** Conceptualization, Supervision, Writing – review & editing, Funding acquisition.

#### Declaration of Competing Interest

The authors declare that they have no known competing financial interests or personal relationships that could have appeared to influence the work reported in this paper.

#### Acknowledgements

This work was supported by the National Research Foundation of Korea (NRF) grant funded by the Ministry of Science and ICT (MSIT), Republic of Korea (No. 2019R1A2C1002400). This work was also supported by the National Research Foundation of Korea (NRF) grant funded by the Korea government (MSIT) (NRF-2021R1C1C1009692).

#### Appendix A. Supporting information

Supplementary data associated with this article can be found in the online version at doi:10.1016/j.apcatb.2022.121226.

#### References

- [1] K. Zeng, X. Zheng, C. Li, J. Yan, J.H. Tian, C. Jin, P. Strasser, R. Yang, Recent advances in non-noble bifunctional oxygen electrocatalysts toward large-scale production, *Adv. Funct. Mater.* 30 (2020), 2000503.
- [2] Z. Chen, X. Duan, W. Wei, S. Wang, B.J. Ni, Recent advances in transition metal-based electrocatalysts for alkaline hydrogen evolution, *J. Mater. Chem. A* 7 (2019) 14971–15005.
- [3] S. Yagi, I. Yamada, H. Tsukasaki, A. Seno, M. Murakami, H. Fujii, H. Chen, N. Umezawa, H. Abe, N. Nishiyama, S. Mori, Covalency-reinforced oxygen evolution reaction catalyst, *Nat. Commun.* 6 (2015) 8249.
- [4] S.H. Ahn, S.J. Hwang, S.J. Yoo, I. Choi, H.J. Kim, J.H. Jang, S.W. Nam, T.H. Lim, T. Lim, S.K. Kim, J.J. Kim, Electrodeposited Ni dendrites with high activity and durability for hydrogen evolution reaction in alkaline water electrolysis, *J. Mater. Chem.* 22 (2012) 15153–15159.
- [5] F. Zhang, R. Ji, Y. Liu, Y. Pan, B. Cai, Z. Li, Z. Liu, S. Lu, Y. Wang, H. Jin, C. Ma, X. Wu, A novel nickel-based honeycomb electrode with microtapered holes and abundant multivacancies for highly efficient overall water splitting, *Appl. Catal. B Environ.* 276 (2020), 119141.
- [6] L. Yang, L. Huang, Y. Yao, L. Jiao, In-situ construction of lattice-matching  $\text{NiP}_2/\text{NiSe}_2$  heterointerfaces with electron redistribution for boosting overall water splitting, *Appl. Catal. B Environ.* 282 (2021), 119584.
- [7] W. Zhu, W. Chen, H. Yu, Y. Zeng, F. Ming, H. Liang, Z. Wang, NiCo/NiCo–OH and NiFe/NiFe–OH core shell nanostructures for water splitting electrocatalysis at large currents, *Appl. Catal. B Environ.* 278 (2020), 119326.
- [8] P. Guo, Z. Wang, T. Zhang, C. Chen, Y. Chen, H. Liu, M. Hua, S. Wei, X. Lu, Initiating an efficient electrocatalyst for water splitting via valence configuration of cobalt-iron oxide, *Appl. Catal. B Environ.* 258 (2019), 117968.
- [9] N.U.A. Babar, Y.F. Joya, H. Khalil, F. Hussain, K.S. Joya, Thin-film iron-oxide nanobeads as bifunctional electrocatalyst for high activity overall water splitting, *Int. J. Hydrog. Energy* 46 (2021) 7885–7902.
- [10] S. Ghosh, B.P. Bloom, Y. Lu, D. Lamont, D.H. Waldeck, Increasing the efficiency of water splitting through spin polarization using cobalt oxide thin film catalysts, *J. Phys. Chem. C* 124 (2020) 22610–22618.
- [11] S. Liu, R.T. Gao, M. Sun, Y. Wang, T. Nakajima, X. Liu, W. Zhang, L. Wang, In situ construction of hybrid  $\text{Co}(\text{OH})_2$  nanowires for promoting long-term water splitting, *Appl. Catal. B Environ.* 292 (2021), 120063.
- [12] P. Babar, A. Lokhande, H.H. Shin, B. Pawar, M.G. Gang, S. Pawar, J.H. Kim, Cobalt iron hydroxide as a precious metal-free bifunctional electrocatalyst for efficient overall water splitting, *Small* 14 (2018), 1702568.
- [13] J.R. McKone, B.F. Sadtler, C.A. Werlang, N.S. Lewis, H.B. Gray, Ni-Mo nanopowders for efficient electrochemical hydrogen evolution, *ACS Catal.* 3 (2013) 166–169.
- [14] M. Gong, W. Zhou, M.J. Kenney, R. Kapusta, S. Cowley, Y. Wu, B. Lu, M.-C. Lin, D.-Y. Wang, J. Yang, B.-J. Hwang, H. Dai, Blending  $\text{Cr}_2\text{O}_3$  into a NiO–Ni electrocatalyst for sustained water splitting, *Angew. Chem.* 127 (2015) 12157–12161.
- [15] Y. Yang, M. Zhou, W. Guo, X. Cui, Y. Li, F. Liu, P. Xiao, Y. Zhang,  $\text{NiCo}_2\text{O}_4$  nanowires grown on carbon fiber paper for highly efficient water oxidation, *Electrochim. Acta* 174 (2015) 246–253.
- [16] B. Zhang, F. Yang, X. Liu, N. Wu, S. Che, Y. Li, Phosphorus doped nickel-molybdenum aerogel for efficient overall water splitting, *Appl. Catal. B Environ.* 298 (2021), 120494.
- [17] S. Piontek, C. Andronescu, A. Zaichenko, B. Konkena, K. Junge Puring, B. Marler, H. Antoni, I. Sinev, M. Muhler, D. Mollenhauer, B. Roldan Cuenya, W. Schuhmann, U.P. Apfel, Influence of the Fe:Ni ratio and reaction temperature on the efficiency of  $(\text{Fe}_x\text{Ni}_{1-x})_2\text{S}_8$  electrocatalysts applied in the hydrogen evolution reaction, *ACS Catal.* 8 (2018) 987–996.
- [18] C. Karakaya, N. Solati, U. Savacl, E. Keleş, S. Turan, S. Çelebi, S. Kaya, Mesoporous thin-film  $\text{NiS}_2$  as an idealized pre-electrocatalyst for a hydrogen evolution reaction, *ACS Catal.* 10 (2020) 15114–15122.
- [19] L. Wu, L. Yu, F. Zhang, B. McElhenny, D. Luo, A. Karim, S. Chen, Z. Ren, Heterogeneous bimetallic phosphide  $\text{Ni}_2\text{P-Fe}_2\text{P}$  as an efficient bifunctional catalyst for water/seawater splitting, *Adv. Funct. Mater.* 31 (2021), 2006484.
- [20] R.B. Wexler, J.M.P. Martirez, A.M. Rappe, Active role of phosphorus in the hydrogen evolving activity of nickel phosphide (0001) surfaces, *ACS Catal.* 7 (2017) 7718–7725.
- [21] P.W. Menezes, C. Panda, S. Loos, F. Bunschei-Bruns, C. Walter, M. Schwarze, X. Deng, H. Dau, M. Driess, A structurally versatile nickel phosphite acting as a robust bifunctional electrocatalyst for overall water splitting, *Energy Environ. Sci.* 11 (2018) 1287–1298.
- [22] X. Li, J. Zhou, C. Liu, L. Xu, C. Lu, J. Yang, H. Pang, W. Hou, Encapsulation of Janus-structured  $\text{Ni/Ni}_2\text{P}$  nanoparticles within hierarchical wrinkled N-doped carbon nanofibers: Interface engineering induces high-efficiency water oxidation, *Appl. Catal. B Environ.* 298 (2021), 120578.
- [23] A.B. Laursen, K.R. Patraju, M.J. Whitaker, M. Retuerto, T. Sarkar, N. Yao, K. V. Ramanujachary, M. Greenblatt, G.C. Dismukes, Nanocrystalline  $\text{Ni}_5\text{P}_4$ : a hydrogen evolution electrocatalyst of exceptional efficiency in both alkaline and acidic media, *Energy Environ. Sci.* 8 (2015) 1027–1034.
- [24] S. Li, C. Yang, Z. Yin, H. Yang, Y. Chen, L. Lin, M. Li, W. Li, G. Hu, D. Ma, Wet-chemistry synthesis of cobalt carbide nanoparticles as highly active and stable electrocatalyst for hydrogen evolution reaction, *Nano Res.* 10 (2017) 1322–1328.
- [25] C. Sun, J. Zeng, H. Lei, W. Yang, Q. Zhang, Direct electrodeposition of phosphorus-doped nickel superstructures from choline chloride-ethylene glycol deep eutectic solvent for enhanced hydrogen evolution catalysis, *ACS Sustain. Chem. Eng.* 7 (2019) 1529–1537.
- [26] A.B. Laursen, R.B. Wexler, M.J. Whitaker, E.J. Izett, K.U.D. Calvino, S. Hwang, R. Rucker, H. Wang, J. Li, E. Garfunkel, M. Greenblatt, A.M. Rappe, G.C. Dismukes, Climbing the volcano of electrocatalytic activity while avoiding catalyst corrosion:  $\text{Ni}_3\text{P}$ , a hydrogen evolution electrocatalyst stable in both acid and alkali, *ACS Catal.* 8 (2018) 4408–4419.
- [27] Q. Liu, C. Tang, S. Lu, Z. Zou, S. Gu, Y. Zhang, C.M. Li, Rationally tuning the atomic ratio of electrodeposited NiP for greatly enhanced hydrogen evolution in alkaline media, *Chem. Commun.* 54 (2018) 12408–12411.
- [28] W. Li, Y. Zhao, Y. Liu, M. Sun, G.I.N. Waterhouse, B. Huang, K. Zhang, T. Zhang, S. Lu, Exploiting Ru-induced lattice strain in CoRu nanoalloys for robust bifunctional hydrogen production, *Angew. Chem. Int. Ed.* 60 (2021) 3290–3298.



- [29] B.K. Kim, S.K. Kim, S.K. Cho, J.J. Kim, Enhanced catalytic activity of electrodeposited Ni-Cu-P toward oxygen evolution reaction, *Appl. Catal. B Environ.* 237 (2018) 409–415.
- [30] Y. Pan, Y. Liu, J. Zhao, K. Yang, J. Liang, D. Liu, W. Hu, D. Liu, Y. Liu, C. Liu, Monodispersed nickel phosphide nanocrystals with different phases: synthesis, characterization and electrocatalytic properties for hydrogen evolution, *J. Mater. Chem. A* 3 (2015) 1656–1665.
- [31] B. Zhang, J. Zhang, X. Tang, Y.H. Lui, S. Hu, An investigation of Fe incorporation on the activity and stability of homogeneous  $(\text{Fe}_x\text{Ni}_{1-x})_2\text{P}$  solid solutions as electrocatalysts for alkaline hydrogen evolution, *Electrochim. Acta* 294 (2019) 297–303.
- [32] B. You, N. Jiang, M. Sheng, M.W. Bhushan, Y. Sun, Hierarchically porous urchin-like  $\text{Ni}_2\text{P}$  superstructures supported on nickel foam as efficient bifunctional electrocatalysts for overall water splitting, *ACS Catal.* 6 (2016) 714–721.
- [33] L. Chai, S. Liu, S. Pei, C. Wang, Electrodeposited amorphous cobalt-nickel-phosphide-derived films as catalysts for electrochemical overall water splitting, *Chem. Eng. J.* 420 (2021), 129686.
- [34] J. Mohammed-Ibrahim, S. Xiaoming, Recent progress on earth abundant electrocatalysts for hydrogen evolution reaction (HER) in alkaline medium to achieve efficient water splitting – a review, *J. Energy Chem.* 34 (2019) 111–160.
- [35] G.B. Darband, M. Aliofkhaizaei, S. Shanmugam, Recent advances in methods and technologies for enhancing bubble detachment during electrochemical water splitting, *Renew. Sustain. Energy Rev.* 114 (2019), 109300.
- [36] M.J. Kim, T. Lim, K.J. Park, S.K. Cho, S.-K. Kim, J.J. Kim, Characteristics of pulse-reverse electrodeposited Cu thin films, *J. Electrochem. Soc.* 159 (2012) D538–D543.
- [37] M.J. Kim, T. Lim, K.J. Park, O.J. Kwon, S.-K. Kim, J.J. Kim, Characteristics of pulse-reverse electrodeposited Cu thin film, *J. Electrochem. Soc.* 159 (2012) D544–D548.
- [38] M.J. Kim, T. Lim, K.J. Park, S.-K. Kim, J.J. Kim, Pulse-reverse electrodeposition of Cu for the fabrication of metal interconnection, *J. Electrochem. Soc.* 160 (2013) D3081–D3087.
- [39] R. Sun, G. Yu, Z. Xie, B. Hu, J. Zhang, X. He, X. Zhang, Influence of hypophosphite on efficiency and coating qualities of electroless Ni-P deposits on magnesium alloy AZ91D, *Int. J. Electrochem. Sci.* 10 (2015) 7893–7904.
- [40] T. Anik, M. Ebn Touhami, K. Himm, S. Schireen, R.A. Belkhamima, M. Abouchane, M. Cissé, Influence of pH solution on electroless copper plating using sodium hypophosphite as reducing agent, *Int. J. Electrochem. Sci.* 7 (2012) 2009–2018.
- [41] Y.E. Sknar, O.O. Savchuk, I.V. Sknar, Characteristics of electrodeposition of Ni and Ni-P alloys from methanesulfonate electrolytes, *Appl. Surf. Sci.* 423 (2017) 340–348.
- [42] B. Bera, A. Chakraborty, T. Kar, P. Leuaa, M. Neergat, Density of states, carrier concentration, and flat band potential derived from electrochemical impedance measurements of N-doped carbon and their influence on electrocatalysis of oxygen reduction reaction, *J. Phys. Chem. C* 121 (2017) 20850–20856.
- [43] Z.H. Xue, H. Su, Q.Y. Yu, B. Zhang, H.H. Wang, X.H. Li, J.S. Chen, Janus Co/CoP nanoparticles as efficient Mott–Schottky Electrocatalysts for overall water splitting in wide pH range, *Adv. Energy Mater.* 7 (2017), 1602355.
- [44] H. Wang, S. Min, Q. Wang, D. Li, G. Casillas, C. Ma, Y. Li, Z. Liu, L.J. Li, J. Yuan, M. Antonietti, T. Wu, Nitrogen-doped nanoporous carbon membranes with Co/CoP Janus-type nanocrystals as hydrogen evolution electrode in both acidic and alkaline environments, *ACS Nano* 11 (2017) 4358–4364.
- [45] F. Cardon, W.P. Gomes, On the determination of the flat-band potential of a semiconductor in contact with a metal or an electrolyte from the Mott-Schottky plot, *J. Phys. D: Appl. Phys.* 11 (1978) L63–L67.
- [46] R. He, J. Hua, A. Zhang, C. Wang, J. Peng, W. Chen, J. Zeng, Molybdenum disulfide-black phosphorus hybrid nanosheets as a superior catalyst for electrochemical hydrogen evolution, *Nano Lett.* 17 (2017) 4311–4316.
- [47] M. Barawi, I.J. Ferrer, J.R. Ares, C. Sánchez, Hydrogen evolution using palladium sulfide (PdS) nanocorals as photoanodes in aqueous solution, *ACS Appl. Mater. Interfaces* 6 (2014) 20544–20549.
- [48] M. Wang, M. Zhang, W. Song, W. Zhong, X. Wang, J. Wang, T. Sun, Y. Tang, A highly stable  $\text{CoMo}_2\text{S}_4/\text{Ni}_3\text{S}_2$  heterojunction electrocatalyst for efficient hydrogen evolution, *Chem. Commun.* 57 (2021) 785–788.
- [49] G. Liu, P. Li, G. Zhao, X. Wang, J. Kong, H. Liu, H. Zhang, K. Chang, X. Meng, T. Kako, J. Ye, Promoting active species generation by plasmon-induced hot-electron excitation for efficient electrocatalytic oxygen evolution, *J. Am. Chem. Soc.* 138 (2016) 9128–9136.
- [50] Y. Huang, X. Zhao, F. Tang, X. Zheng, W. Cheng, W. Che, F. Hu, Y. Jiang, Q. Liu, S. Wei, Strongly electrophilic heteroatoms confined in atomic CoOOH nanosheets realizing efficient electrocatalytic water oxidation, *J. Mater. Chem. A* 6 (2018) 3202–3210.
- [51] S. Huang, Z. Jin, P. Ning, C. Gao, Y. Wu, X. Liu, P. Xin, Z. Chen, Y. Jiang, Z. Hu, Z. Chen, Synergistically modulating electronic structure of  $\text{NiS}_2$  hierarchical architectures by phosphorus doping and sulfur-vacancies defect engineering enables efficient electrocatalytic water splitting, *Chem. Eng. J.* 420 (2021), 127630.
- [52] A. Ray, S. Sultana, L. Paramanik, K.M. Parida, Recent advances in phase, size, and morphology-oriented nanostructured nickel phosphide for overall water splitting, *J. Mater. Chem. A* 8 (2020) 19196–19245.
- [53] A.R.J. Kucernak, V.N. Naranammampuram Sundaram, Nickel phosphide: the effect of phosphorus content on hydrogen evolution activity and corrosion resistance in acidic medium, *J. Mater. Chem. A* 2 (2014) 17435–17445.
- [54] H. Cheshideh, F. Nasirpour, Cyclic voltammetry deposition of nickel nanoparticles on  $\text{TiO}_2$  nanotubes and their enhanced properties for electro-oxidation of methanol, *J. Electroanal. Chem.* 797 (2017) 121–133.
- [55] J. Rongé, T. Dobbelaere, L. Henderick, M.M. Minjauw, S.P. Sree, J. Dendooven, J. A. Martens, C. Detavernier, Bifunctional earth-abundant phosphate/phosphide catalysts prepared: Via atomic layer deposition for electrocatalytic water splitting, *Nanoscale Adv.* 1 (2019) 4166–4172.